Journal Name

Imaging and Analysis of Covalent Organic Framework Crystallites on a Carbon Surface: Nanocrystalline Scaly COF/Nanotube Hybrid[†]

Benjamin L. Weare,[a] Rhys W. Lodge,[a] Nikolai Zyk,[a] Andreas Weilhard,[a] Claire L. Housley,[a] Karol Strutyński,[b] Manuel Melle-Franco,[b] Aurelio Mateo-Alonso,[c] and Andrei N. Khlobystov[a]

Synthesis of covalent organic frameworks (COFs) is well-advanced but understanding their nanoscale structure and interaction with other materials remains a significant challenge. Here we have developed a methodology for the detailed imaging and analysis of COF crystallites using carbon nanotubes substrates for COF characterisation. Detailed investigation using powder X-ray diffraction, infrared spectroscopy, mass-spectrometry and scanning electron microscopy in conjunction with a local probe method, transmission electron microscopy (TEM), revealed details of COF growth and nucleation at the nanoscale. A boronate ester COF undergoes preferential growth in the *a-b* crystallographic plane under solvothermal conditions. Carbon nanotubes were found to not impact the mode of COF growth, but the crystallites on nanotubes were smaller than COF crystallites not on supports. COF crystalline regions with sizes of tens of nanometres exhibited preferred orientation on nanotube surfaces where the c-axis is oriented between 50-90 ° relative to the carbon surface. The COF/nanotube hybrid structure was found to be more complex than the previously suggested concentric core-shell model, and can be better described as a nanocrystalline scaly COF/nanotube hybrid.

Introduction

Covalent organic frameworks (COFs) are polymeric ordered solids made by joining organic molecules with strong, covalent bonds using the principles of dynamic covalent chemistry (DCC). The first COFs were made of sub-units linked with boroxine and boronate ester bonds respectively.[1] COF chemistry has since expanded to include a range of heteroatomic building blocks, for example; (i) nitrogen-containing bonds such as imines,[2] imides,[3] phenazines,[4] beta-ketoenamines,[5] triazines,[6] hydrazones[7] and amides;[8] (ii) alternative boron bonds such as spiroborates[9] and borosilicates;[10] and (iii) a range of other covalent linkers such as olefins[11] and dioxins.[12] COFs are remarkable for their low-density (due to light elements C, B, O H and N), high-surface area and porosity, and can have a 3D or 2D topology with regard to the covalent lattice.[13] These properties enable COF to be utilised in an array of applications; such as heterogeneous catalysis,[14] energy storage,[15] gas sorption and storage,[16] and biomedical applications.[17,18] COFs may be synthesised by a variety of methods, typically using solvothermal synthesis,[19] but ionothermal,[6] sonochemical,[20] microwave[21] and mechanochemical[22] syntheses have also been used to deliver high-quality COF materials.

Building COF synthesis around reversibly formed bonds allows crystalline COFs to form using the error-checking process, were lattice defects are "corrected" via dynamic bond breaking and reforming.[23] Despite this, COFs are often synthesised as paracrystalline powders (having a short-range but lacking a long-range crystal structure) materials with macroscopic single-crystal COFs only recently achieved.[24] Two significant approaches have been employed to improve the crystallinity of COFs; firstly, the inclusion of modulators that reversibly compete with the COF monomers to promote the formation of the thermodynamically favoured crystalline lattice rather than the kinetically favoured acrystalline lattice;[25] and secondly, the inclusion of reagents, such as pyridine for boron-containing COFs, that facilitate the reverse reaction in the error-checking process.[26]

The reversible nature of COF bonds poses major challenges of chemical stability (compared to materials made by irreversible polymerisation) and lack of processability. In particular, boron-based COFs tend to hydrolyse in the presence of water, leading to

a School of Chemistry, University of Nottingham, Nottingham, NG7 2RD, United Kingdom.
b CICECO - Aveiro Institute of Materials, Department of Chemistry, University of Aveiro, 3810-193 Aveiro, Portugal.
c POLYMAT, University of the Basque Country UPV/EHU, Avendia de Tolosa 72, E-20018 Donostia-San Sebastian, Spain.
† Electronic Supplementary Information (ESI) available: Additional information is available as Word Document containing selected area electron diffraction patterns, tabulated data for infrared spectra, mass spectra, electron diffraction, TEM measurements and calculated binding energies, and the equations used. See DOI: 00.0000/00000000.

a loss of crystallinity or a complete loss of the COF lattice.[27] Furthermore, most COFs are formed as powders which are difficult to incorporate into real-world devices.

To overcome these issues, COFs can be combined with a support material. This approach makes them more applicable by mitigating their instability, as well as improving their manipulation and processability properties.[28] Synthesis of hybrids can be achieved by a top-down approach, such as delamination of COF sheets and subsequent stacking onto a support,[29] or by a bottom-up approach where the COF forms directly on the support substrate. A variety of supports have been employed, such as graphene,[30] hexagonal boron-nitride,[31] metal nanowires[32] and carbon nanotubes.[33]

Carbon nanotubes (CNTs) are a particularly effective support for COFs because they are easy to manipulate and can be successfully incorporated into devices.[34] CNTs may be single-walled (SWNTs), double-walled (DWNTs) or multiwalled (MWNTs). The largest MWNTs are known as graphitised nanofibers (GNFs), and are CNTs that have an external MWNT enveloping corrugated graphitic sheets that form an internal step-edge structure.[35,36] The quasi-1D topology of nanotubes, combined with high thermal and electrical conductivity, a broad spectrum of light absorption, and outstanding chemical, mechanical and thermal stability can in principle be passed on to the COF materials by creating a functional and exploitable COF/nanotube hybrid material.

COF/nanotube hybrids have been synthesised using solvothermal conditions in the presence of nanotubes. This approach has been proven to be amenable to a variety of COFs, both 2D and 3D, and the suitability of these hybrids has been tested for a range of applications including electrochemical sensing[37,38] and energy storage.[33,39] However, understanding the structural relationship between COFs and nanotubes at the nano scale has remains a challenge. While bulk-scale techniques, such as powder X-ray diffraction (PXRD) and infrared (IR) spectroscopy, are excellent tools for investigating the structure and properties of COFs, they cannot probe the COF-nanotube interface within the hybrid material. Transmission electron microscopy (TEM) is an excellent local-probe technique for nanoscale analysis as it can give rich structural information;[40] COF/nanocarbon composite formation mechanisms and structure can be interrogated and the interfaces between the support and the COF can be investigated. However, TEM is mainly used to infer the presence of COF on a nanoscale substrate, without deeper structural analysis and investigation of the COF lattice with regards to the support lattice. The current "core-shell" model proposed for COF/nanotube hybrids[41–45] is a useful initial step towards understanding the interface between the two materials, which in future can help to establish molecular mechanisms of COF formation on supports and uncover synergistic interactions between their structures at the single-molecule level.

Here we present a nanoscale structural investigation of a hybrid material consisting of a boronate ester COF on the surface of GNFs. We established an experimental methodology, combining bulk- and local-probe techniques that allow us to determine important structural characteristics of the COF/nanotube hybrid material that have implications for future advancement of this class of materials.

Results and Discussion

A novel COF isostructural to Marta-COF-1[46] and Marta-COF-2[47] was synthesised from cata-hexamethoxyhexabenzocoronene (cHBC) and benzene-1,2-diboronic acid (BDA), with the inclusion of phenylboronic acid (PBA) as a modulator (Figure 1a). The cHBC-BDA(98)-PDA(2)-COF (referred to hereafter as COF) was synthesised using a solvent system that has been used to successfully synthesise crystalline boronate ester COF nanoparticles.[48] The reaction conditions were chosen after iterative syntheses to improve crystalinity and provide COF thin enough for TEM imaging. Without inclusion of a modulator, the COF was found to have fewer nanocrystallites in TEM. The COF product was analysed by attenuated total reflectance infrared (ATR-IR) spectroscopy (Figure 2a), which shows the formation of boronate ester rings due to the presence of characteristic vibrations as well as boronic acid stretches (1393, 1333, 1235, 1079, 660, 601 and 541 cm^{-1}), whilst boroxine and cHBC OH vibrational modes are absent (SI, Table S1). The spectrum is fully consistent with that of Marta-COF-2.[49] This suggests that the COF is composed of a lattice joined by boronate ester bonds and terminated by boronate esters of BDA and PBA. Matrix-assisted laser desorption-ionisation time-of-flight mass spectrometry (MALDI-ToF MS) was carried out on the COF (Figure 2b) and showed the presence of ions that corresponded to cHBC nodes joined by BDA linkers and fragments thereof, in agreement with simulated isotope patterns and confirmed the molecule composition of the new COF (SI, Table S2). Below the cHBC molecular ion peak (696 m/z), the MALDI spectrum of COF is dominated by cHBC and its fragmentation products.

TEM was used to acquire direct-space images of the COF (Figure 3a, b). To prevent degradation of the COF lattice, the TEM samples were prepared without solvent by rolling the TEM grid in the dry COF powder, and imaging was performed at 80 kV to mitigate electron beam damage via direct-knock-on effects[50] and at low electron dose-rate, thus extending the lifetime of the COFs under the electron-beam. The micrographs reveal that the COF consists of nanoscale crystalline regions with lattice-fringes corresponding to projection of columns of cHBC nodes. Stacked polyaromatic moieties in columns of cHBC are the region of greatest density in the COF lattice thus providing the most mass-thickness contrast in TEM images, and clearly demarcating the direction of COF pore channels in each nano-crystallite. Hexagonal projections down the *c*-axis, where each vertex is a column of cHBC nodes, provided a face-on view of the COF pore; the measured pore diameter of 3.0 - 3.7 nm is consistent with the predicted diameter of 2.8 - 4.0 nm in proposed model simulations (Figure 1b). Changes in COF crystallite orientation so the c-axis in not perpendicular to the e-beam exhibit different distances between the columns of cHBC nodes in projection (Figure 4). Analysis of the inter-column spacing (Figure 4a) reveals a bimodal distribution, showing two groups of distances between 2.4 - 3.8 nm and 1.5 - 2.1 nm. Correlation of TEM images with 3D structural models of the COF indicates that the first larger group corresponds to COF
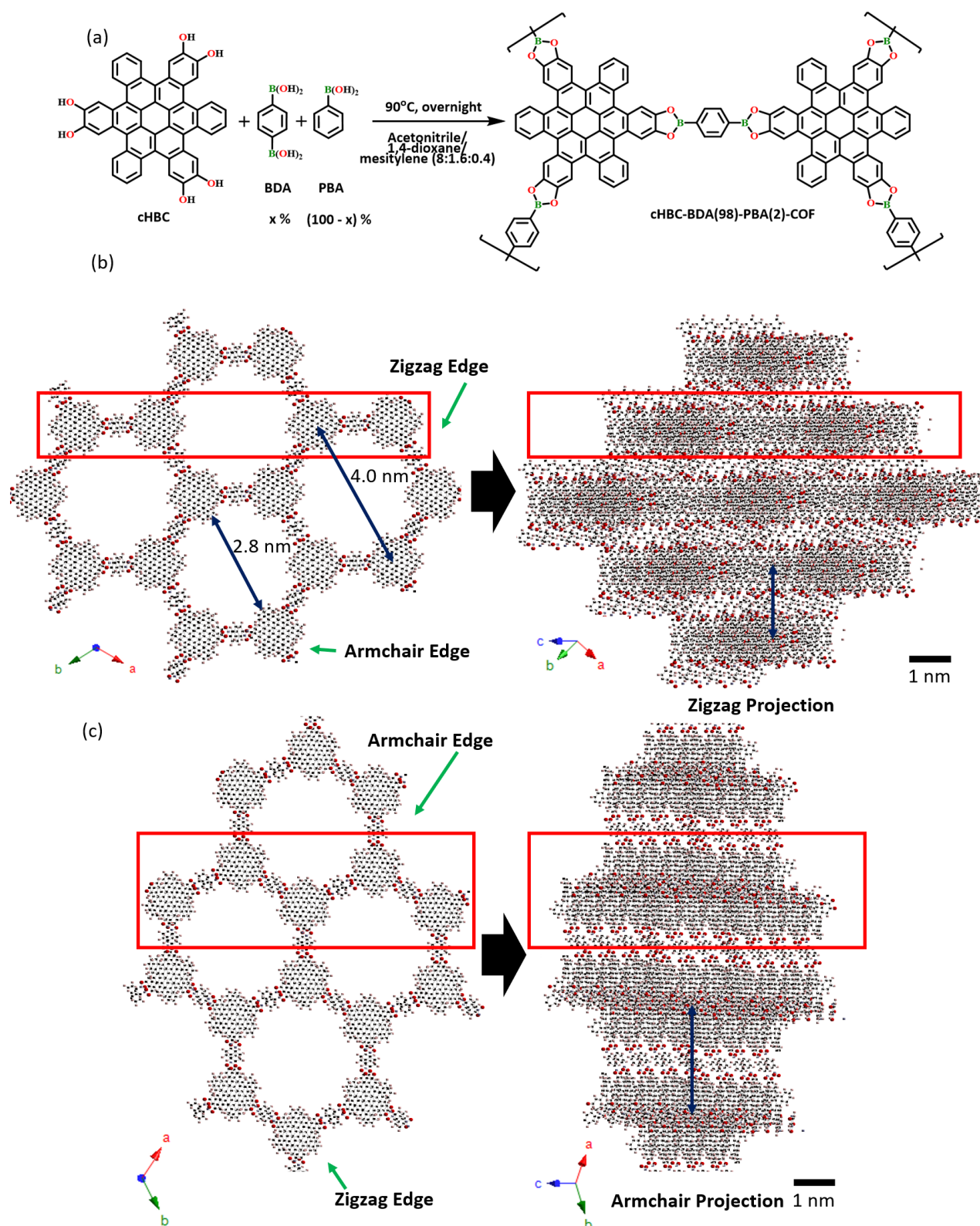
Fig. 1 (a) COF synthetic scheme showing the boronate ester linkage formed. Structural diagram of COF sheets in the armchair (b) and zigzag (c) orientations and the same structures rotated by 50° in the a/b plane. The a (red) and b (green) axes are indicated parallel to the page, with the c axis (blue) perpendicular to the page. Columns of stacked cHBC nodes are highlighted by red boxes, and the projection distance between the mid-points of columns is shown by blue arrows; 3.0 nm for the armchair direction and 1.9 nm for the zigzag direction. The simulated structures contain 8 COF layers. The modelled unit cell assumes a P1 space group where a = 3.48 nm, b= 3.49 nm, c = 0.81 nm, α = 88.6 °, β =87.1 ° and γ = 118°. The pore diameter, indicated by blue arrows, is 4.0 nm when measured from the centre of a cHBC node to the centre of the opposite node and is 2.8 nm when measured from the edge of a cHBC node to the edge of the opposite node.
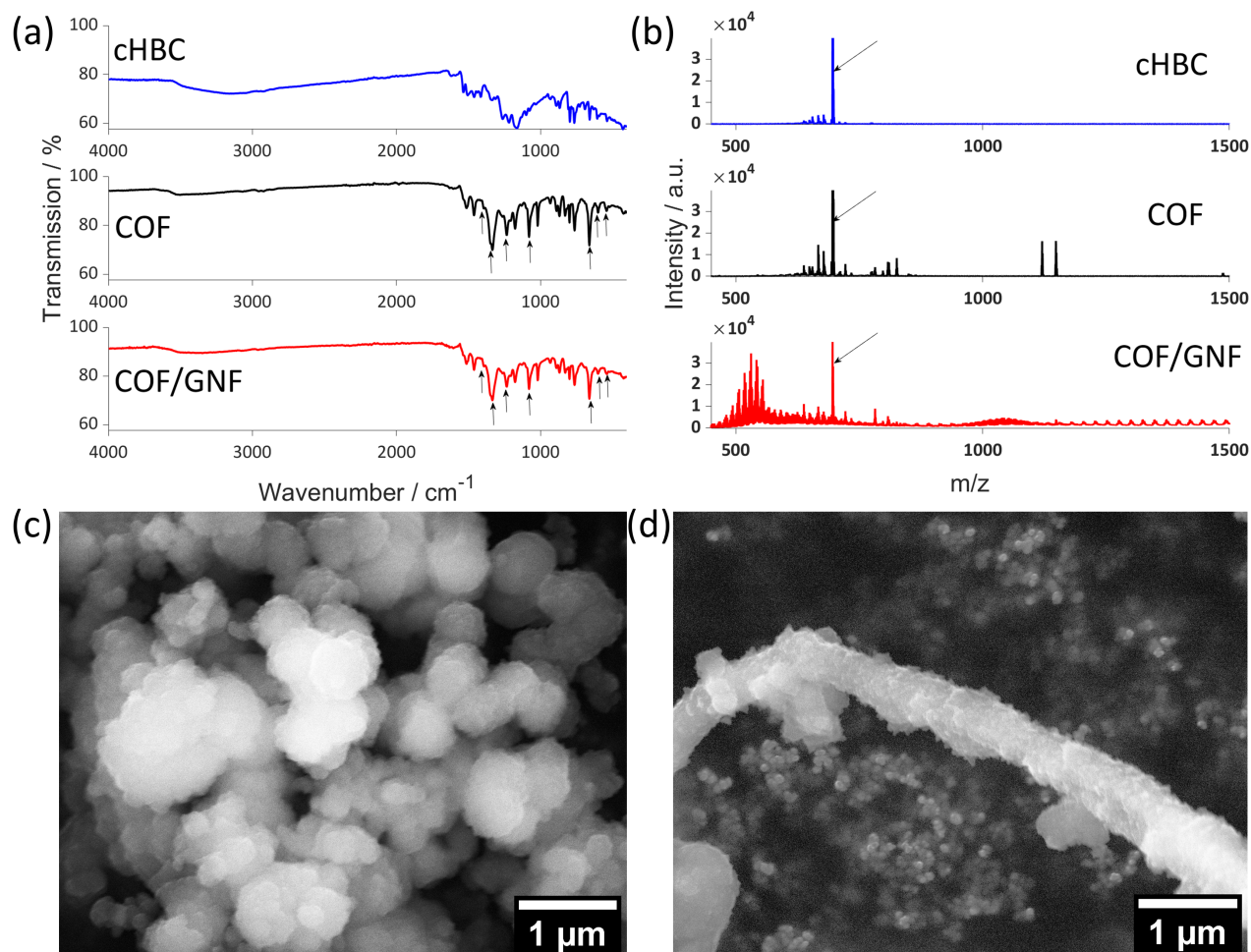
Fig. 2 (a) Top: ATR-IR spectra of cHBC (blue), neat COF (black) and COF/GNF hybrid (red). COF and COF/GNF show characteristic boronate ester stretches indicated with black arrows at 1393, 1333, 1235, 1079, 660, 601 and 541 cm^{-1}. (b) Positive-ion MALDI mass spectra of COF (black), COF/GNF hybrid (red) and cHBC (blue) all without matrix. The peak at 696 m/z indicated by a black arrow was due to a singly charged cHBC ion; below 700 m/z, the spectra were dominated by fragments arising from cHBC; above 700 m/z, the COF and COF/GNF spectra contains singly charged ions that correspond to cHBC nodes joined by BDA linkers, and fragments thereof. For COF/GNF, above 1000 m/z the spectrum was dominated by carbonaceous peaks separated by 24 m/z caused by laser induced fragmentation of the GNF, which serve to mask peaks arising from the COF lattice. (c) SEM image of COF. (d) SEM image COF/GNF hybrid.
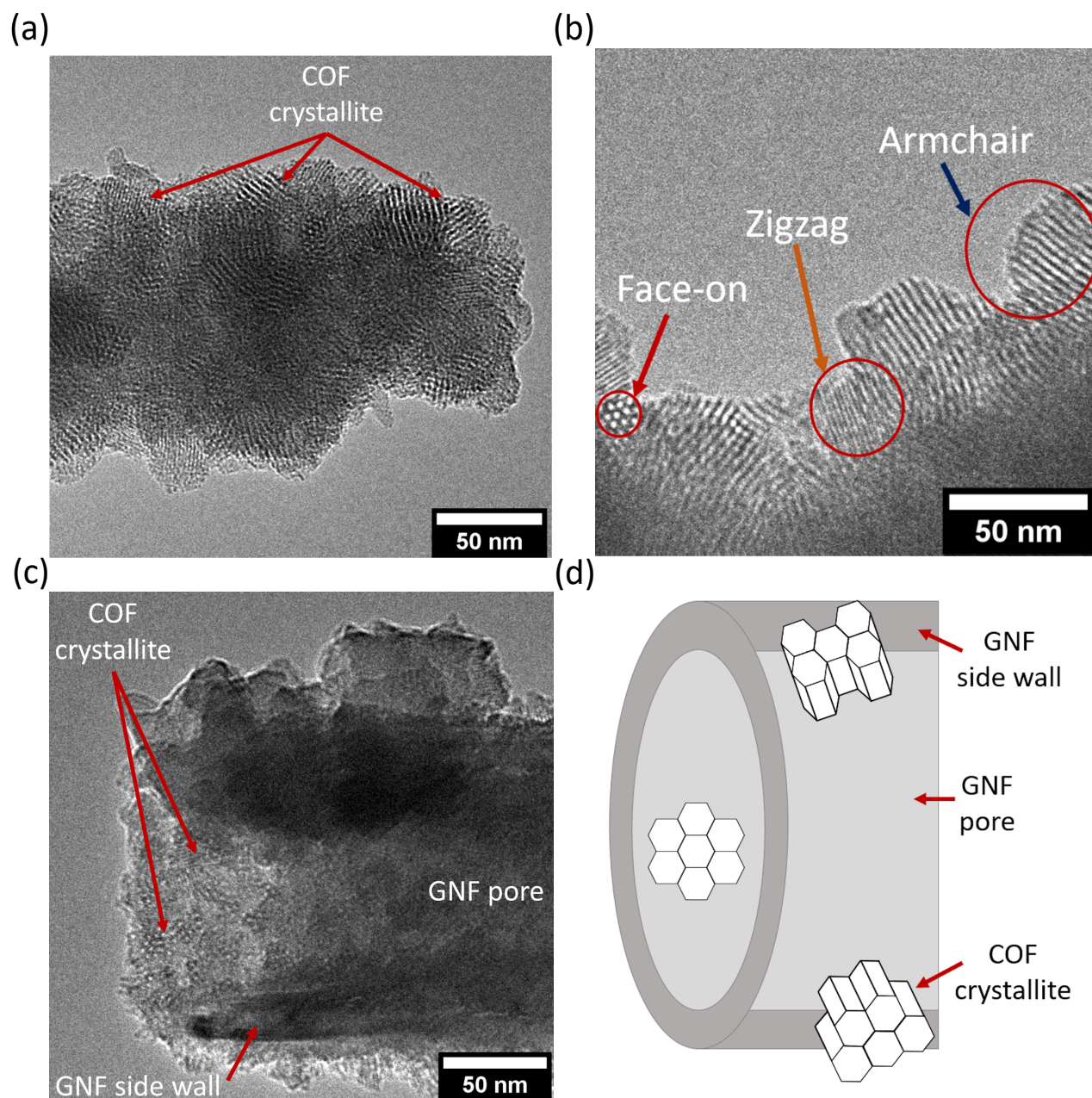
Fig. 3 TEM micrograph of COF material, demonstrating irregular morphology and random orientation of nano-crystalline regions and (b) illustrating the face on projection, and the parallel (orange) and perpendicular (blue) directions of the COF crystallites. (c) TEM micrograph of COF/GNF, showing irregular morphology of COF nanocrystallites grown on graphitic surfaces and illustrating the GNF pore and graphitic side wall. (d) Diagram illustrating the structure of COF/GNF hybrid, including the location of the GNF pore, the GNF graphitic side walls and the COF crystallites. The crystallites are shown in an armchair, zigzag and face-on projection.

particles projected along the armchair direction with the zigzag direction perpendicular to the e-beam (Figure 1c); the second smaller group to COF projected along the zigzag direction with the armchair direction perpendicular to the electron beam (Figure 1b). Plainly, the spacing observed changes depending on whether the armchair or zigzag edge of the COF is aligned with the optical axis of the TEM. This is because the image-forming process in TEM creates a parallel projection on a 2D plane of a 3D structure. The observed spread in the distribution of intercolumnar spacings is due to the deviation of crystallite orientation from the principal armchair or zigzag orientations. Consistent with Marta-COF-1, interlayer spacing along the *c*-axis corresponding to the separation between the 2D COF sheets cannot be observed by direct-space imaging due to the non-planar, wavy nature of the stacked COF sheets in this type of material.[46] Of note is that TEM analysis of Marta-COF-2, prepared under non-optimised conditions and without inclusion of PBA modulator, was unable to resolve the same level of detail and yield less structural information than in this work.

Measurements of the COF crystallite size (Figures 4b, c) were taken parallel and perpendicular to the COF pore channels, which revealed that the crystallites tended to extend further perpendicular to the pore channels. The modal crystallite size for parallel growth (determined from histogram in Figure 4c) was 14-16 nm with the greatest being 52.5 nm. The modal crystallite size for perpendicular growth was 20-24 nm with the greatest being 59.9 nm. This suggests that the COF structure grows more rapidly by addition to an existing COF sheet, rather than by formation of a new COF layer by π-π stacking of COF monomers on top of an existing sheet (i.e. faster in the *a-b* crystal plane). The nanocrystallites are observed alongside non-crystalline regions in the COF structure (Figure 3a), indicating it is a paracrystalline material, having short but lacking long-range order.

To further investigate the crystal structure of the COF, selected-area electron diffraction (SAED) and powder X-ray diffraction (PXRD) were employed (SI, Figures S1 and S2). The SAED pattern contains some diffuse rings, which do not correspond to any d-spacing observed in the direct-space TEM micrographs (SI, Table S3). However, they match well with the rings observed in the SAED pattern of GNFs and also with literature values for graphitic carbon,[51] suggesting they originate from graphitic-type carbon present in the sample such as the carbon film of the TEM grid. This implies that the COF crystallites are not strongly Bragg diffracting the electron beam and the diffraction is caused by trace graphitic carbon in the sample, or that under SAED conditions the structure degrades rapidly into a graphitic material. Interestingly, while increasing the electron dose to yield a sharper diffraction pattern, no sharp diffraction pattern was observed for the free COF. This implies that the COF is not strongly diffracting, rather than being unstable under the electron-beam. It can be assumed that bright-field imaging and SAED impart a similar electron-dose as long as brightness is not adjusted; the COF structure is stable for some minutes at the dose-rate used for bright field imaging, but a useful diffraction pattern is not recorded under these conditions. Increasing brightness in SAED must increase the electron dose, so it becomes more likely that the COF struc-

ture will be degraded by the e-beam due to an increased electron dose, but a transient diffraction pattern that fades quickly over time would be expected if the COF was strongly diffracting and degrading under the beam.

The PXRD pattern (SI, Figure S2) suggests that the COF material is paracrystalline with broad peaks seen at $2\theta = 17.9$ º, 23.8 º, 26.5 º and 28.4 º in the experimental diffractogram, and diffuse background characteristic of amorphous material. The Scherrer equation (SI, Equation S1) was applied to the measured crystallite sizes (τ) and calculated Bragg angles (θ) (using Cu(Kα_1) radiation = 1.5046 Å (λ) and a shape factor (K) of 1 to predict line broadening (β) in the PXRD. For the largest and smallest measured crystallites (59.9 nm and 12.9 nm), the predicted line broadening is 6.8 º and 1.8 º respectively. Applying the Scherrer equation to the observed peak at 5.1 º with a value of $\beta = 7.26 \times 10^{-3}$ rad gives a predicted crystallite size of 21.2 nm. This value is within the range of crystallite sizes measured in TEM. For the peak at 23.8 º, $\beta = 3.14 \times 10^{-3}$ rad and $\tau = 50.1$ nm which is also consistent with the size of crystallites observed in TEM, thus supporting that the broad PXRD peaks at $2\theta = 5$ º and 7 º may correspond to the spacings along the zigzag and armchair channels of COF nanocrystallites. These results differ from the PXRD obtained for Marta-COF-1, which gave a diffraction pattern containing clear sharp peaks that readily matched the simulated powder pattern. Assuming Marta-COF-1 and COF are isostructural, this further demonstrates the lack of observable long-range crystallinity in COF.

Computational modelling of cHBC and COF on graphene surfaces was undertaken to give insight into the formation of COF/GNF hybrids (Figure 5a, SI Table S5). Graphene is a suitable model for the surface of a GNF because from the point of view of a cHBC molecule, the curvature of a GNF (taken as the reciprocal of the radius) is negligible over short distances. A GNF of radius 75 nm would have a curvature of 0.013 nm^{-1}, while curvature of cHBC is 0.86 nm^{-1} (Figure 5b). It was found that cHBC has a large binding energy to graphene (-2.139 eV) that is very close to the modelled binding energy of cHBC to cHBC (-2.074 eV). The binding energy to graphene of a COF fragment consisting of two cHBC units joined by a BDA linker (cHBC-BDA-cHBC) (-2.109 eV) was very close to the binding energy of cHBC. This was due to the corrugated geometry of the COF sheet that allowed only one cHBC unit to sit on the graphene surface (Figure 5). For the COF unit cell, graphene is a suitable model for the GNF surface as over the length of the unit cell, the curvature of a GNF is negligible. Modelling the extended COF structure on graphene found the binding energy of one COF layer on graphene (-2.202 eV) was lower than the binding energy between two AA stacked COF sheets (-5.221 eV), indicating a single COF layer on a graphitic support surface is unlikely. Furthermore, it was found that by modelling COF as a planar structure, binding energy increased to a value comparable to AA stacking (-5.142 eV) due to increased contact area between the molecule and the graphene surface. These results suggest that cHBC and COF moieties will readily attach to the surface of graphitic carbon supports (such as GNFs), facilitating the growth of COF on the support surface. However, the large binding energy suggests that desorption of
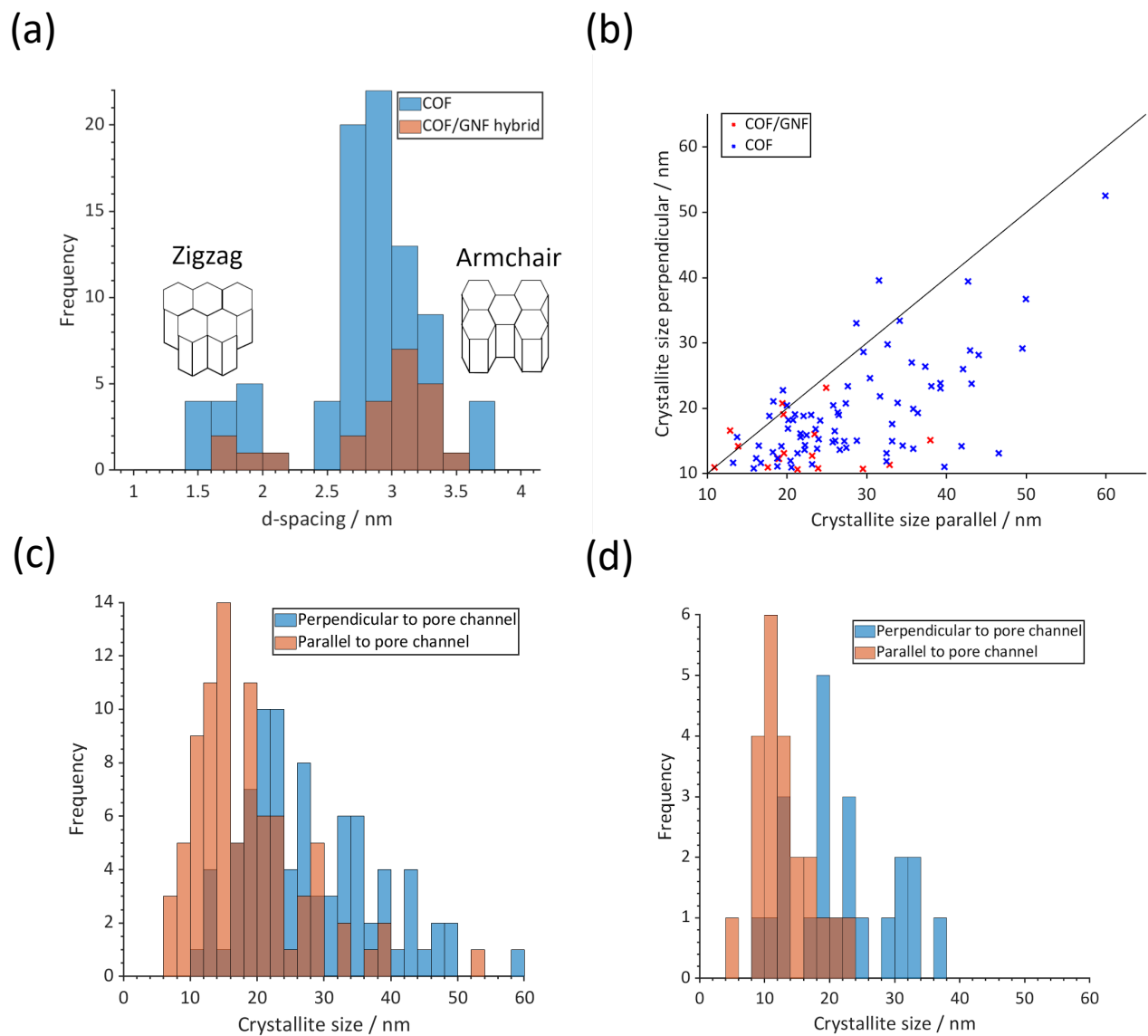
Fig. 4 (a) d-Spacing distribution histogram for free COF (blue, 87 measurements taken from 15 micrographs) and COF/GNF hybrid (orange, 23 measurements taken from 9 micrographs). For both materials, the bimodal distribution contains a group of distances between 1.4 and 2.1 nm corresponding to projections of COF nanocrystals along the armchair direction and a group between 2.4 and 3.8 nm corresponding to projections along the zigzag direction. The mean and sample standard deviation (2σ) for free COF is 2.8 ± 1.1 nm and for COF/GNF is 2.9 ± 1.1 nm. (b) Scatter plot showing crystallite size perpendicular and parallel to the COF pore channels for COF (blue) and COF/GNF (red). The black fit line is for $y = x$, such that any point which falls on the line indicates a crystallite of equal dimensions. For both COF and COF/GNF more points fall below the line than above, indicating that the crystallites measured are larger perpendicular to the COF pore channels than parallel. (c) COF crystallite size distribution and (d) COF/GNF hybrid crystallite size distributions. Crystallite sizes were measured as the largest dimension perpendicular to the pore channel (blue) and the largest measurement parallel to the pore channel (orange) (COF: 85 measurements from 15 micrographs; COF/GNF: 22 measurements from 9 micrographs). The mean and sample standard deviations (2σ) were: COF; 28 ± 20 nm (perpendicular), 18 ± 16 nm (parallel); COF/GNF; 22 ± 16 nm (perpendicular), 13 ± 8.0 nm (parallel). For both materials, crystallites tended to have their largest dimension perpendicular to the COF pore channels.
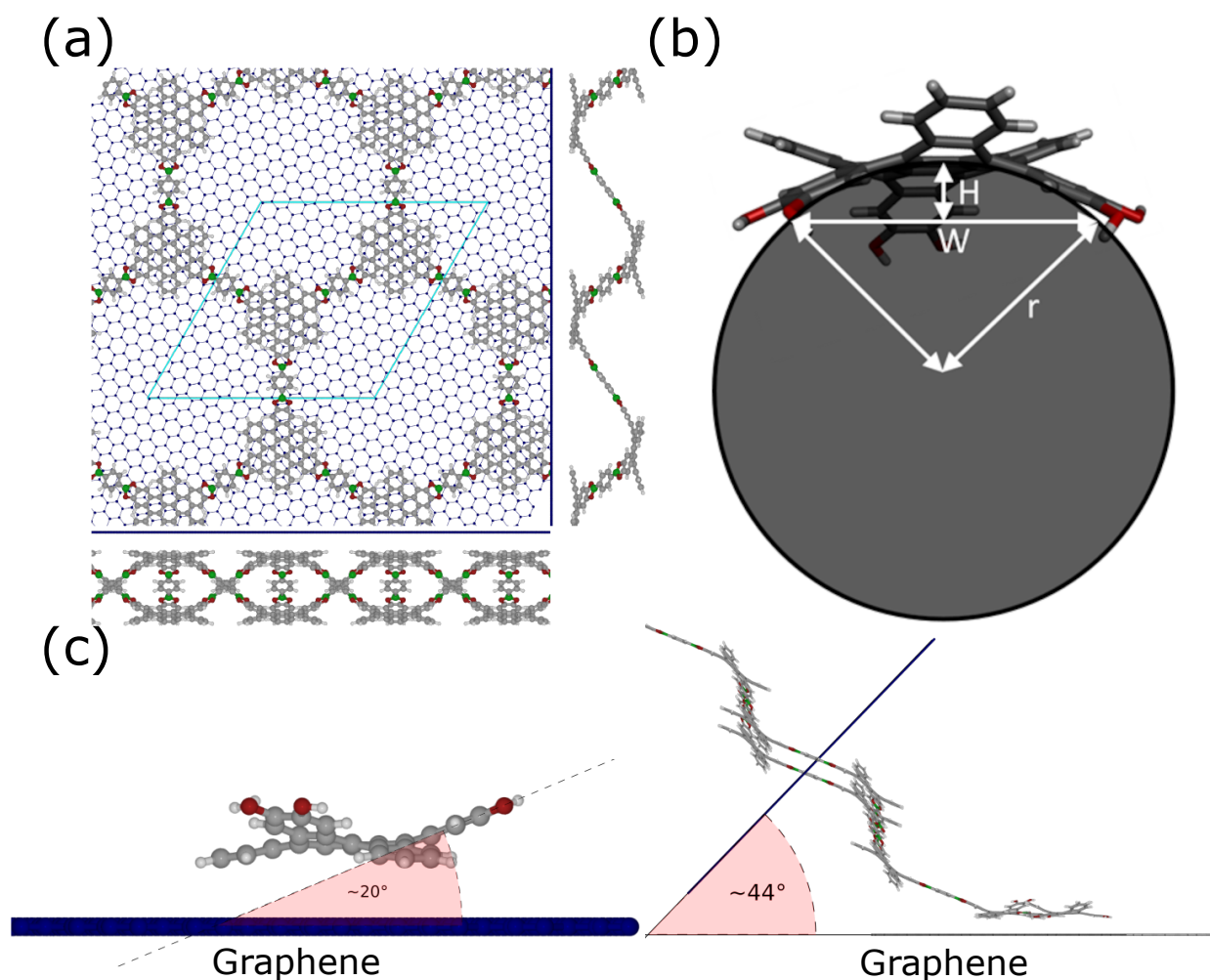
Fig. 5 (a) COF unit cell modelled on graphene, viewed from above and the sides. (b) Diagram of intersecting chords theorem, used to calculated the radius of a sphere on which cHBC could fit and the curvature of cHBC as the reciprocal radius. W is the width of the chord, the distance between opposite hydroxyl groups, H is the height of the chord and r the radius of the sphere. (c) Illustration of angle between graphene surface (blue line) and hydroxy groups of cHBC (20°) and of the angle between graphene surface and COF pore channel (44°).

cHBC and COF from the graphitic surface is unlikely, impeding the correction of defects in the growing COF lattice when it adsorbed on a carbon surface. Modelling the orientation of cHBC nodes in COF relative to the graphene surface found that pore channels would be 44º relative to the graphene surface.

COF/GNF hybrids were made under the same conditions as COF, by including GNF in the reaction mixture during the COF growth step to yield a black powder. The difference in colour to pure COF, a green powder, is due to the GNFs being opaque across the visible spectrum. Despite GNFs also absorbing strongly across the IR spectrum, ATR-FTIR of COF/GNF (Figure 2a) clearly shows the presence of the same characteristic boronate ester vibrations seen in free COF (Figure 2a). The presence of COF in the hybrid material was further confirmed by MALDI-ToF MS (Figure 2b), which showed the same ion fragments as pure COF as well as extra peaks due to the GNF acting as a matrix and assisting in the desorption-ionisation of the COF lattice.[52]

Scanning electron microscopy (SEM) imaging revealed the mi-

croscale structure of COF/GNF hybrid (Figure 2c, d). The micrographs showed that COF formed approximately spherical microparticles which conglomerate to form the thick structures with thin edges seen in TEM. Common crystal morphologies such as needles or plates were not observed, confirming that COF lacks long-range order. The COF/GNF hybrid sample contained both COF microparticles and GNFs covered within an irregular layer of COF, as was expected from the TEM. These observations suggest that COF forms readily on nanocarbon structures, but does not do so exclusively or preferentially.

Direct-space TEM imaging was employed to investigate the nanoscale structure of COF/GNF hybrid (Figure 3c, d). This revealed that the sample contained both free COF, and COF absorbed on GNF (COF/GNF hybrid). As for the pure COF sample, the COF/GNF hybrid had an irregular, angular morphology with visible lattice-fringes. When crystallite sizes for COF on the GNF surface were measured, the crystalline domains tended to be larger perpendicular to the COF pore channels. The measured
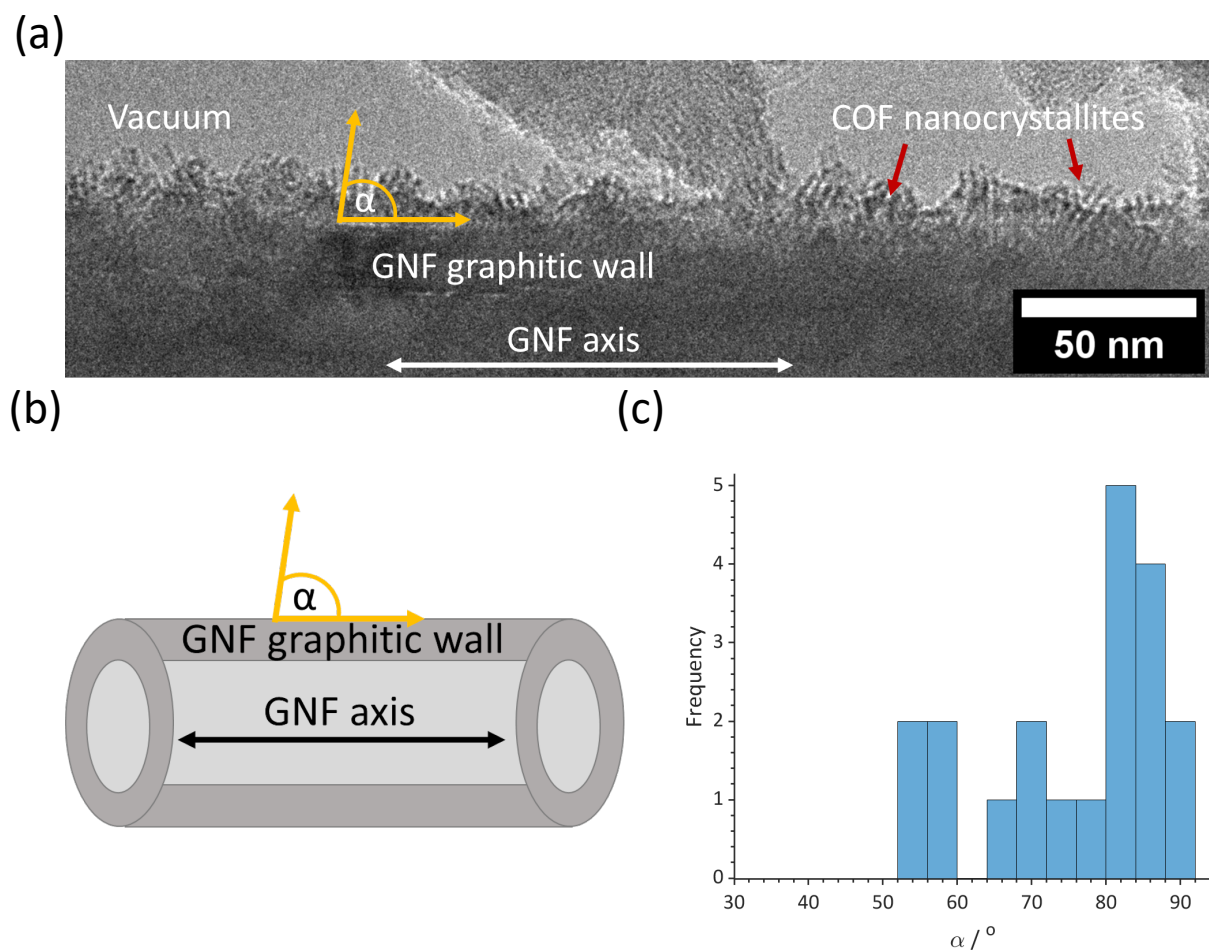
Fig. 6 (a) Measurement of COF pore channel angle, where y is the direction of the COF pore channel, x is the direction of the GNF surface and α is the angle between them and (b) diagram illustrating the same. (c) COF@GNF angle distribution histogram (20 measurements from 9 images). A variety of angles between 52 ° and 90 ° were measured, with COF pore channels tending towards 90 degrees. The mean and sample standard deviation (2σ) is 75 ± 24 °. No COF pore channels were observed parallel to the GNF surface (0 °).

lattice spacings of the COF/GNF hybrid match well with those of pure COF (Figures 4b-d). As with the COF, a series of distances corresponding to the COF pore channels were observed in conjunction with hexagonal COF pores. While generally smaller than pure COF, the COF/GNF crystallites were also on the order of tens of nanometres (Figure 4d). The modal crystallite size by parallel growth was 10-12 nm with the greatest being 20.7 nm. The modal crystallite size by perpendicular growth was 18-20 nm with the greatest being 33.1 nm. Measurements where taken of the angle between the COF pore channels and the surface of the GNF (Figure 6). It was found that the COF pore channels varied between 52 ° and 90 °, but were never observed to be parallel to the GNF surface (crystallographic c-axis) (Figure 6). These observations imply that the COF monomers adhere to the GNF surface via π-π stacking, rather than associating with the GNF through hydrogen bonding to the GNF π-system. From the shape of the COF crystallites, it can be concluded that the COF sheets grow along the surface of the GNF faster than they grow out from it (in the direction of the pore channels), similar to what is seen in free

COF. This is consistent with the computational results, which suggested that competition would occur between COF growth across and GNF surface and as stacked COF sheets would be competitive as there was no signicant difference between the binding energy for cHBC to a graphene surface and to a cHBC molcule. Therefore, there is no clear thermodynamic advantage to either grow process, leading to the observed small, disordered crystallites.

Being a low-throughput local-probe method, statistical analysis of TEM images must be done methodically to ensure that the analysis is meaningful and representative of the bulk material. Comparison between the datasets for free COF and COF/GNF (Figures 4, SI Table S4) show that both have a comparable mean lattice spacing and standard distribution of 2.8 ± 1.1 nm (COF) and 2.9 ± 1.1 nm (COF/GNF), indicating the observed distances fall within a well-defined range despite differences in sample size between the two sets which indicating that the presence of GNF does not cause alterations to the COF unit cell. The distributions show that COF nanocrystallites in COF/GNF tend to be oriented along the armchair lattice projection (i.e. with the zigzag lat-

tice projection parallel to the curvature of the GNF). This is may be an effect of sample size, as COF particles and GNF are distributed randomly on the TEM grid, and the amount of armchair and zigzag COF observed would be expected to converge as the number of measurements made increases. Similar to free COF, the largest measured crystallite size in COF/GNF is perpendicular to the pore channel. For both sets, the most frequently measured size range corresponded to a larger crystallite size for the perpendicular measurement, seen by the mode being higher in value for the perpendicular measurements in COF and COF/GNF (Figure 5). The crystallite size distributions are all unimodal and skewed towards the lower sizes, as is expected for a step-growth polymer.[53] In this case, crystallite domain size distribution is a proxy for the molecular weight distribution and qualitatively shows that the COF polymer can be considered quite polydisperse. This data indicates similar growth behaviour for free COF and COF/GNF hybrid; formation of crystallites on the order of tens of nanometres, that grow larger perpendicular to the pore channels than parallel. Smaller crystallites were more common than larger ones, indicating that the COF begins growth at many points simultaneously to form many crystallites of which few achieve larger sizes. Free COF crystallites sizes cover a larger range than COF/GNF crystallites but have a comparable smallest crystallite size for both sets of measurements, which supports the previous conclusion that COF crystallites grow from many points at once in both samples, and shows that crystallites in COF/GNF hybrids do not reach as large a size as free COF crystallites.

It has been previously suggested that COF/nanotube hybrids have a "core-shell" structure, where a continuous COF sheet wraps around the GNF in a uniform coaxial arrangement.[41–45] Our detailed structural analysis of COF/GNF hybrid demonstrates that the "core-shell" concentric model is an oversimplification. The surface of the nanotube is rather scattered with discrete particles of COF where their channels adopt a range of angles between 50-90 º indicating a complex structural relationship, but with the prevalent crystalline orientation corresponding to face-on attachment of the COF lattice to the carbon lattice. Being structurally uniform and extending for some micrometres, GNF surfaces provide a number of identical nucleation sites to initiate COF growth such that COF is expected to begin growth at many points of the GNF at once. Thus, lack of long-range crystallinity in COF on GNF surfaces can be better explained by the COF growing at several points simultaneously on the surface of the GNF to form short-range ordered crystallites due to strong and irreversible adsorption of cHBC monomers on GNF surface nucleating the crystallites. These crystallites will then merge and overlap as they grow towards one another, giving multiple crystalline domains with regions of acrystallinity between them.[54] The COF in this scenario can be visualised as overlapping scales on an ancient Roman *lorica squamata*,[55] and it is proposed these hybrids be known as "scaly COF". As the pores of the COF scales remain open and oriented approximately perpendicular to the GNF surface, ensuring access of molecules and ions to the carbon surface as well as good contact with the polyaromatic columns of stacked cHBC, the COF/GNF hybrid is expected to possess useful functional electronic and electrochemical properties that could be exploited in electrocatalysis and battery materials.

Conclusions

Features of covalent organic frameworks are complex and polydisperse but are often oversimplified in the current structural considerations for these types of materials. Our boronate ester COF revealed a paracrystalline structure with crystallite size in the range of 20-60 nm, and preferential direction of particle growth along the covalent COF layer (*a-b* crystal plane) including slight anisotropy in the shape of nanocrystallites. Direct-space TEM imaging in the direction perpendicular to the c-axis enabled the analysis of orientations of nanocrystallites of COF, showing a preferential alignment along the zigzag direction of the COF sheet. The same COF material grown on the surface of graphitised carbon nanofibers showed only subtle structural differences to the free COF, but a strong correlation of COF nanocrystallite orientations with respect to the underlying graphitic carbon lattice. This indicated a preferential perpendicular arrangement of COF channels to the surface driven by π-π interactions between polyaromatic building blocks of the COF and the graphitic surface. Modelling using graphene as a simplified analogue of GNFs found that the binding energies of cHBC to cHBC and graphene were very close, leading to the observed competition between COF growth laterally on the the surface of the GNF and outwards from the GNF as stacked COF sheets. In contrast to the previous suggestion, that COF layers wrap uniformly around the cylindrical carbon surface of nanotubes, we demonstrated the formation of discontinuous, scaly nanocrystalline morphology of COF/GNF hybrid which has implications for exploitation of functional physiochemical properties of this type of material. Both modelling and experimental results suggest scaly COF crystallites may grow on other 2D support structures.

Experimental

General

Synthesis was carried out using standard laboratory practice with Pyrex glassware with reagents bought from Merck, Alfa-Aesar, Fischer Scientific or Acros Organics and used without further purification unless explicitly stated. cHBC was synthesised as cata-hexamethoxyhexabenzocoronene via the literature procedure and deprotected before COF syntheses.[56][57]

All ^{1}H and ^{13}C NMR spectroscopy was performed on a Bruker Ascend 400HD. IR spectra were recorded on solids using a Bruker Alpha FTIR Spectrometer using a Bruker Platinum ATR attachment over the range 4000-600 cm^{-1}.

MALDI-ToF MS measurements were recorded using a Bruker ultraFlexIII (Bruker Daltonik, Bremen, Germany). Samples were dispersed in acetone or chloroform without a matrix unless otherwise indicated then drop-cast onto a stainless steel target plate (type MTP384; Bruker Daltonik, Bremen, Germany). The sample was ionised using a pulsed solid-state UV laser (355 nm, 500 μJ, 66.7 Hz). The instrument was operated in linear mode with data being acquired using the on-board flexControl software (v3, B185;Bruker Daltonik, Bremen, Germany) and processed using Bruker's flexAnalysis software (v3, B96; Bruker Daltonik, Bremen,

Germany).

Powder X-ray diffraction measurements were made with a PANalytical Xpert Pro using Cu(Kα_1) radiation ($\lambda = 1.5432$ Å) from 2 º - 40 º 2θ on a zero-background silicon holder in Bragg-Brentano geometry.

Scanning electron microscopy (SEM) images were taken using a JEOL 7100F field emission gun scanning electron microscope. Samples were prepared on a 10 mm aluminium stub with an adhesive carbon tab. Imaging was conducted at a working distance of 10 mm and accelerating voltage of 15 kV.

Transmission electron microscopy (TEM) and selected-area electron diffraction (SAED) were performed using a JEOL 2100PLUS transmission electron microscope with an accelerating voltage of 80 kV located at the University of Nottingham Nanoscale and Microscale Research Centre. COF and COF@GNF samples were prepared via bringing a copper TEM grid coated with "lacey" carbon film (Agar Scientific UK) into contact with the dry powdered sample and gently agitating the sample against the grid for 1 minute. Analysis was performed using Gatan Microscopy Suite 3 and ImageJ FIJI software.[58,59]

Calculations

Tight Binding (TB) calculations were used to explore different conformations and to preoptimise COF as well as to study in detail COF/graphene interfaces. The Matsci parameter set with attractive dispersion corrections from the OPLSAA force-field as implemented on the DFTB+ software was used.[60,61] The COF periodic structure was computed with DFT with the Fritz Haber Institute ab initio molecular simulations (FHI-aims) package with "light" numeric atomic orbitals, which approximately correspond to TZVP Gaussian type orbitals.[62–64] The PBE functional augmented with Many Body Dispersion (MBD) was used for geometry optimisation and energies.[65,66] 3D images of the modelled structures were prepared using CrystalMaker (ver 2.07).

COF synthesis

Cata-Hexahydroxyhexabenzocoronene (4.7 mg, 6.75×10^{-3} mmol), benzene-para-diboronic acid (1.76 mg, 1.06×10^{-2} mmol,98.5 mol%) and phenylboronic acid (1.9 mg, 1×10^{-3} mmol,1.5 mol%) were combined with a mixture of acetonitrile/dioxane/mesitylene (8 mL/1.6 mL/0.4 mL). The solids were dispersed by sonicating for 15 mins, then the mixture was syringe filtered (PTFE, 2.5 μm) and degassed via 3 freeze-pump-thaw cycles. The green reaction mixture was heated at 90 ºC overnight. The solid green product was collected via filtering under reduced pressure, then was washed with THF (10 mL), then acetone (10 ml) and then hexane (10 mL). The dry green product was stored under reduced pressure in the presence of a desiccant (1.9 mg, 1×10^{-3} mmol, 16.8 %). MS (MALDI-ToF) m/z 1487 (0.7 %), 1149 (7.1), 1121 (7.1), 864.1 (0.3), 853.9 (0.4), 850.1 (0.55), 826.1 (3.7) 810.3 (2.8), 798.1 (1.2), 782.1 (1.9), 775.9 (1.0), 733.9 (0.75), 722.0 (2.5), 712.0 (1.1), 710 (0.89), 696.0 (M$^+$, 100), 693.9 (3.0), 677.9 (5.1), 666.8 (6.4), 655.1(2.0), 648.9 (2.0), 637.9 (2.2). IR (ATR)ν_{max} / cm^{-1}: 3501br (OH), 1393w (CO$_2$B), 1334s (BC), 1235s (CO), 1079vs (BO), 660.7vs (BO),

599.2w (CO2B), 539.7w (OH).

COF/GNF hybrid synthesis

GNFs (1.9 mg) were dried at 400 ºC for 1 hour. cata-Hexahydroxyhexabenzocoronene (9.8 mg,0.0147 mmol), benzene-para-diboronic acid (3.4 mg,0.0205 mmol, 83.4 mol%) and phenylboronic acid (0.5 mg, 0.0041 mmol, 16.6 mol%) were combined with a mixture of acetonitrile/dioxane/mesitylene (8 mL/1.6 mL/0.4 mL). The solids were dissolved by sonicating for 15 mins, then the mixture was syringe filtered (PTFE, 2.5 μm), mixed with GNF, then degassed via 3 freeze-pump-thaw cycles. The green reaction mixture was heated at 90 ºC overnight. The solid green product was collected via filtering under reduced pressure, then was washed with THF (10 mL), then acetone (10 mL) and then hexane (10 mL). The dry black product was stored under reduced pressure in the presence of a desiccant (10.9 mg). MS (MALDI-ToF) m/z . IR (ATR)ν_{max} / cm^{-1}: 3347br (OH), 1393w (CO$_2$B), 1334s (BC), 1235s (CO), 1079vs (BO), 660.7vs (BO), 601.2w (CO$_2$B), 539.7w (OH). MS (MALDI-ToF) m/z 1180 (7.1 %), 1149 (9.5), 1132 (6.5), 1111 (7.0), 936.2 (5.5), 912.2 (5.3), 891.2 (5.7). 867.2 (5.6), 833.5 (5.7), 826.2 (2.0), 819.1 (5.9), 808.2 (13.1), 798.1 (7.8), 750.1 (7.8), 734.0 (10), 722.0 (18), 714.1 (11), 696 (M$^+$, 100), 678 (18), 667 (23), 649 (17), 637.9 (26), 624.9 (18), 603 (17), 591 (20), 578.9 (20), 565.9 (23), 554.98 (53), 543.9 (67) 541.9 (67), 530.9 (82), 517.9 (60), 506.8 (42), 493.8 (25), 480.8 (14), 467.8 (7.4).

Conflicts of interest

There are no conflicts to declare.

Acknowledgements

Notes and references

1 A. P. Côté, A. Benin, N. W. Ockwig, M. O'Keeffe, A. J. Matzger and O. M. Yaghi, *Science*, 2005, **310**, 1166–1170.

2 S. Wan, F. Gándara, A. Asano, H. Furukawa, A. Saeki, S. K. Dey, L. Liao, M. W. Ambrogio, Y. Y. Botros, X. Duan, S. Seki, J. F. Stoddart and O. M. Yaghi, *Chem. Mater*, 2011, **23**, 4094–4097.

3 Q. Fang, Z. Zhang, S. Gu, R. B. Kaspar, J. Zheng, J. Wang, S. Qiu and Y. Yan, *Nat. Commun.*, 2014, **5**, 4503.

4 J. Guo, Y. Xu, S. Jin, L. Chen, T. Kaji, Y. Honsho, M. A. Addicoat, J. Kim, A. Saeki, H. Ihee, S. Seki, S. Irle, M. Hiramoto, J. Gao and D.Jiang, *Nat. Commun.*, 2013, **4**, 2736.

5 M. R. Rao, Y. Fang, S. D. Feyter and D. F. Perepichka, *J. Am. Chem. Soc.*, 2017, **139**, 2421–2427.

6 P. Kuhn, M. Antonietti and A. Thomas, *Angew. Chem. Int. Ed.*, 2008, **47**, 3450–3453.

7 F. J. Uribe-Romo, C. J. Doonan, H. Furukawa, K. Oisaki and O. M. Yaghi, *J. Am. Chem. Soc.*, 2011, **133**, 11478–11481.

8 P. J. Waller, S. J. Lyle, T. M. O. Popp, C. S. Diercks, J. A. Reimer and O. M. Yaghi, *J. Am. Chem. Soc.*, 2016, **138**, 15519–15522.

9 Y. Du, H. Yang, J. M. Whiteley, S. Wan, Y. Jin, S.-H. Lee and W. Zhang, *Angew. Chem. Int. Ed.*, 2015, **128**, 1769–1773.

10 S. Diercks and O. M. Yaghi, *Science*, 2017, **355**, 923–931.

11 H. Lyu, C. S. Diercks, C. Zhu and O. M. Yaghi, *J. Am. Chem. Soc.*, 2019, **141**, 6848–6852.

12 B. Zhang, M. Wei, H. Mao, X. Pei, S. Alshmimri, J. A. Reimer and O. M. Yaghi, *J. Am. Chem. Soc.*, 2018, **140**, 12715–12719.

13 A. Nagai, *Covalent Organic Frameworks*, Jenny Stanford Publishing, 2020, pp. 10–11.

14 S.-Y. Ding, J. Gao, Q. Wang, Y. Zhang, W.-G. Song, C.-Y. Su and W. Wang, *J. Am. Chem. Soc.*, 2011, **133**, 19816–19822.

15 S. Dalpati, M. Addicoat, S. Jin, T. Sakurai, J. Gao, H. Xu, S. Irle, S. Seki and D. Jiang, *Nat. Commun.*, 2015, **6**, 7786.

16 Y. Li and R. T. Yang, *AlChE J.*, 2007, **54**, 269–279.

17 Q. Fang, J. Wang, S. Gu, R. B. Kaspar, Z. Zhuang, J. Zheng, H. Guo, S. Qiu and Y. Yan, *J. Am. Chem. Soc.*, 2015, **137**, 8352–8355.

18 P. Bhanja, S. Mishra, K. Manna, A. Mallick, K. D. Saha and A. Bhaumik, *ACS Appl. Mater. Interfaces*, 2017, **9**, 31411–31423.

19 H. L. Nguyen, N. Hannikel, S. J. Lyle, C. Zhu, D. M. Proserpio and O. M. Yaghi, *J. Am. Chem. Soc*, 2020, **142**, 2218–2221.

20 S.-T. Yang, J. Kim, H.-Y. Cho, S. Kim and W.-S. Ahn, *RSC Adv.*, 2012, **2**, 10179–10181.

21 N. L. Campbell, R. Clowes, L. K. Ritchie and A. I. Cooper, *Chem. Mater.*, 2009, **21**, 204–206.

22 B. P. Biswal, S. Chandra, S. Kandambeth, B. Lukose, T. Heine and R. Banerjee, *J. Am. Chem. Soc.*, 2013, **135**, 5328–5331.

23 A. P. Côté, H. M. El-Kaderi, H. Furukawa, J. R. Hunt and O. M. Yaghi, *J. Am. Chem. Soc.*, 2007, **129**, 12917–12915.

24 T. Ma, E. A. Kapustin, S. X. Yin, L. Liang, Z. Zhou, J. Niu, L.-H. Li, Y. Wang, J. Su, J. Li, X. Wang, W. D. Wang, W. Wei, J. Sun and O. M. Yaghi, *Science*, 2048, **361**, 48–52.

25 S. Wang, Z. Zhang, H. Zhang, A. G. Rajan, N. Xu, Y. Yang, Y. Zeng, P. Liu, X. Zhang, Q. Mao, Y. He, J. Zhao, B.-G. Li, M. S. Strano and W.-J. Wang, *Matter*, 2019, **1**, 1–14.

26 Y. Du, K. Mao, P. Kamakoti, B. Wooler, S. Cundy, Q. Li, P. Ravikovitch and D. Calabro, *J. Mater. Chem. A.*, 2013, **1**, 13171–13178.

27 L. M. Lanni, R. W. Tilford, M. Bharathy and J. J. Lavigne, *J. Am. Chem. Soc.*, 2011, **133**, 13975–13983.

28 W. Zhao, L. Xia and X. Liu, *CrystEngComm*, 2018, **20**, 1613–1634.

29 I. Berlanga, M. L. Ruiz-Gonzàlez, J. M. Gonzàlez-Calbert, J. L. G. Fierro, R. Mas-Ballesté and F. Zamora, *small*, 2011, **7**, 1207–1211.

30 Z. Zha, L. Xu, Z. Wang, X. Li, Q. Pan, P. Hu and S. Lei, *ACS Appl. Mater. Interfaces*, 2015, **7**, 17837–17843.

31 S. Kim and H. C. Choi, *ACS Omega*, 2020, **5**, 948–958.

32 Y. Han, N. Hu, S. Liu, Z. Hou, J. Liu, X. Hua, Z. Yang, L. Wei, L. Wang and H. Wei, *Nanotechnology*, 2017, **28**, 33LT01.

33 X. Chen, H. Zhang, C. Ci, W. Sun and Y. Wang, *ACS Nano*, 2019, **13**, 3600–3607.

34 L. Sacco, S. Florel, I. Florea and C.-S. Cojocaru, *Carbon*, 2020, **157**, 631–639.

35 M. A. Astle, G. A. R. F. M. W. Fay, S. Notman, M. R. Sambrook and A. N. Khlobystov, *J. Mater. Chem. A*, 2018, **6**, 20444–20453.

36 R. W. Lodge, G. A. Rance, M. W. Fay and A. N. Khlobystov, *Nanoscale*, 2018, **10**, 19046–19051.

37 Y. Sun, L. Xu, G. I. N. Waterhouse, M. Wang, X. Qiao and Z. Xu, *Sens. Actuators B Chem.*, 2019, 107–114.

38 L. Wang, Y. Xie, Y. Yang, H. Liang, L. Wang and Y. Song, *ACS Appl. Nano. Mater.*, 2020, **3**, 1412–1419.

39 T. Sun, J. Xie, W. Guo, D.-S. Li and Q. Zhang, *Adv. Energy Mater.*, 2020, **10**,.

40 S. Park, Z. Liao, B. Ibarlucea, H. Qi, H.-H. Lin, D. Becker, J. Melidonie, T. Zhang, H. Sahabudeen, L. Baraban, C.-K. Baek, Z. Zheng, E. Zschech, A. Fery, T. Heine, U. Kaiser, G. Cuniberti, R. Dong and X. Feng, *Angew. Chem. Int. Ed.*, 2020, **59**, 8218–8224.

41 J. Yoo, S.-J. Cho, G. Y. Jung, S. H. Kim, K.-H. Choi, J.-H. Kim, C. K. Lee, S. K. Kwak and S.-Y. Lee, *ACS Nano Lett.*, 2016, **16**, 3292–3300.

42 Z. Lei, Q. Yang, Y. Xu, S. Guo, W. Sun, H. Liu, L.-P. Lv, Y. Zhang and Y. Wang, *Nat. Commun.*, 2018, **9**, 576.

43 B. Sun, J. Liu, A. Cao, W. Song and D. Wang, *Chem. Commun.*, 2017, **53**, 6303–6306.

44 F. Xu, S. Jin, D. Wu, X. Yang, X. Chen, H. Wei, R. Fu and D. Jiang, *Sci. Rep.*, 2015, **5**, 8225.

45 R. Gomes and A. J. Bharracharyya, *ACS Sustain. Chem. Eng.*, 2020, **8**, 5946–5953.

46 M. Martínez-Abadía, C. T. Stoppiello, K. Strutyński, B. Lerma-Berlanga, C. Martí-Gastaldo, A. Saeki, M. Melle-Franco, A. N. Khlobystov and A. Mateo-Alonso, *J. Am. Chem. Soc.*, 2019, **141**, 14403–14410.

47 M. Martínez-Abadía, K. Strutyński, C. T. Stoppiello, B. Lerma-Berlanga, C. Martí-Gastaldo, A. N. Khlobystov, M. Melle-Franco and A. Mateo-Alonso, accepted 2021.

48 A. M. Evans, L. R. Parent, N. C. Flanders, R. P. Bisbey, E. Vitaku, M. S. Kirschner, R. D. Schaller, L. X. Chen, N. Gianneschi and W. R. Dichtel, *Science*, 2018, **361**, 52–57.

49 M. K. Smith and B. H. Northrop, *Chem. Mater.*, 2014, **26**,.

50 S. T. Skowron, I. V. Lebedeva, A. M. Popov and E. Bischoutskaia, *Nanoscale*, 2013, **5**, year.

51 J. Fayos, *J. Solid State Chem.*, 1999, **148**, 278–285.

52 C. Pan, S. Xu, L. Hu, X. Su, J. Ou, H. Zou, Z. Guo, Y. Zhang and B. Guo, *J. Am. Soc. Mass. Spetrom.*, 2005, **16**, 883–892.

53 E. S. Sterner, *J. Chem. Edu.*, 2019, **96**, 2003–2008.

54 H. Qi, H. Sahabudeen, B. Liang, M. Poloźij, M. A. Addicoat, T. E. Gorelik, M. Hambsch, M. Mundszinger, S.-W. Park, B. V. Lotsch, S. C. B. Mannsfeld, Z. Zheng, R. Dong, T. Heine,

X. Feng and U. Kaiser, *Science*, 2020, **6**, eabb5976.

55 M. McCarthy, M. Bishop and T. Richardson, *Antiquity*, 2001, **75**, 507–508.

56 Q. Zhang, H. Peng, G. Zhang, Q. Lu, J. Chang, Y. Dong, X. Shi and J. Wei, *J. Am. Chem. Soc.*, 2014, **136**, 5057–5064.

57 J. McOmie, M. Watts and D. West, *Tetrahedron*, 1968, **24**, 2289 – 2292.

58 J. Schindelin, C. T. Rueden, M. C. Hiner and K. W. Eliceiri, *Mol. Reprod. Dev.*, 2015, **82**, 518–529.

59 J. Schindelin, I. Arganda-Carreras, E. Frise, V. Kaynig, M. Longair, T. Pietzschn, S. Preibisch, C. Rueden, S. Saalfed, B. Schmid, J.-Y. Tinevez, D. J. White, V. Hartenstein, K. Eliceiri, P. Tomancak and A. Cardona, *Nature Methods*, 2012, **9**, 676–682.

60 W. L. Jorgensen and J. Tirado-Rives, *J. Am. Chem. Soc.*, 1988, **110**, 1657–1666.

61 W. L. Jorgensen, D. S. Maxwell and J. Tirado-Rives, *J. Am. Chem. Soc.*, 1996, **118**, 11225–11236.

62 V. Blum, R. Gehrke, F. Hanke, P. Havu, V. Havu, X. Ren, K. Reuter and M. Scheffler, *Comput. Phys. Commun.*, 2009, **180**, 2175–2196.

63 A. Marek, V. Blum, F. Hanke, P. Havu, V. Havu, X. Ren, K. Reuter and M. Scheffler, *J. Phys. Condens. Matter*, 2014, **26**, 213201.

64 V. W. z. Yu, F. Corsetti, A. García, W. P. Huhn, M. Jacquelin, W. Jia, B. Lange, L. Lin, J. Lu, W. Mi, A. Seifitokaldani, A. Vázquez-Mayagoitia, C. Yang, H. Yang and V. Blum, *Comput. Phys. Commun.*, 2018, **26**, 267–285.

65 A. Tkatchenko, R. A. DiStasio, R. Car and M. Scheffler, *Phys. Rev. Lett.*, 2012, **108**, 236402.

66 A. Ambrosetti, A. M. Reilly, R. A. DiStasio and A. Tkatchenko, *J. Chem. Phys.*, 2014, **140**, 18A508.